SPECIAL ISSUE RESEARCH ARTICLE

Aluminum impregnated zinc oxide engineered poly(vinylidene fluoride hexafluoropropylene)-based flexible nanocomposite for efficient harvesting of mechanical energy

Shewli Pratihar | Epsita Kar | Shrabanee Sen

Functional Materials and Devices
Division, CSIR-Central Glass and Ceramic
Research Institute, Kolkata, India

Correspondence
Shrabanee Sen, Functional Materials and
Devices Division, CSIR-Central Glass and
Ceramic Research Institute, Kolkata
700032, West Bengal, India.
Email: shrabanee@cgcri.res.in

Summary

Confronting the depletion of fossil fuel energy as well as pollution generated from chemical batteries, associated with the increasing number of electronic equipment and the internet of things, results in a high requirement of light-weight, low cost, sustainable, and durable power devices. Currently, a flexible and self-powered piezoelectric energy harvester (PZEH) is a suitable alternative, which may be easily integrated with small electronics to realize real-time sustainable energy generation. Therefore, a novel PZEH has been fabricated at room temperature (30°C) using Al-doped ZnO (Al@ZnO) incorporated poly(vinylidene fluoride-hexafluoropropylene) (PVDF-HFP) nanocomposites. Al@ZnO enables nucleation of electroactive phase within PVDF-HFP (10PALZO) exhibited polarity at a much higher fraction (F[EA] >90%) compared to neat PVDF-HFP (F[EA] = 63.8%). Piezoelectric energy harvesting capability of the device has been investigated under gentle repeated human finger tapping. Optimized Al@ZnO-PVDF-HFP composite (with 10 wt% loading)-based PZEH delivered a high value of open-circuit output voltage ∼22 V. Such high output value infers a good energy conversion efficiency of the device. For further enhancement of the performance of the device, the 10PALZO nanocomposite was placed under a high electric field of 2.4 MVcm^{-1} resulting in an open circuit output voltage of ∼26 V. In addition to that, the proposed nanocomposite exhibits a good energy storage efficiency (10PALZO-P) which further enhanced to 111.2 μJcm^{-3} (at 1 Hz) after poling under an electric field 2.4 MVcm^{-1}. This increment in the output value is due to the improved polarization induced by Al@ZnO within the PVDF-HFP matrix. These results highlight that the filler can efficiently maximize the device performance thereby developing new efficient energy harvesting materials.

KEYWORDS
dielectric, ferroelectric, green energy harvester, piezoelectric nanogenerator energy storage

1 | INTRODUCTION

Green energy harvesting techniques from the ambient environment are categorized based on natural energy sources such as solar, thermal, electromechanical, and mechanical.[1-5] Among the different conversion methods piezoelectric nanogenerator (NG) is a powerful and upcoming approach for converting low-frequency mechanical energy into electricity that works through the piezoelectric potential created by an externally applied strain in a piezoelectric material for driving the flow of electrons to the external load.[6,7] Recently human-motion-based piezoelectric energy harvesters (PZEH) have attracted tremendous interest due to their potential applications in portable, embedded, and wearable smart electronics that require a self-sufficient and sustainable power source.[8,9]

Owing to their remarkable piezoelectric, ferroelectric and dielectric properties poly(vinylidene fluoride) (PVDF) and its co-polymer-based nanocomposite films are considered the smart options to be chosen for fabricating piezoelectric NGs.[10-13] Recently several fillers are being used to develop such PZEH. PVDF-based nanocomposites containing nanofillers such as $BaTiO_3$,[14] $ZnSnO_3$,[15] $FAPbBr_3$,[7] RGO:Fe,[16] PZT,[17] Ce^{3+}/graphene,[18] and graphene-silver[19] were utilized to obtain improved output performance of NG. For instance, A $BaTiO_3$@PVDF-TRFE-based PZEH with a maximum output voltage of ~59.5 V and current of 6.52 µA has been reported by Cho et al[20] In addition to that, Zhu et al have fabricated a five layer black phase $CsPbI_3$@PVDF composite which exhibited a voltage output of ~26 V with current density 1.1 µA/cm² and power of ~25 µW.[21] A significantly enhanced value of output voltage has been reported by Muduli et al (output voltage ~83 V, short circuit current of 1.62 µA, and maximum instantaneous power density 142 mW m⁻²) using flexible PVDF-[0.67 $(BiFeO_3)$-0.33$(BaTiO_3)$]-based PZEH.[22] They also fabricated PVDF-$ZnSnO_3$-MoS_2-based nanocomposite, which can produce an open-circuit voltage of 26 V, short circuit current of 0.5 µA, and an instantaneous power density and 28.9 mW m⁻², respectively.[23] Ga-PZT@GaO_x has been used as a filler in PVDF-TrFE to design a wearable PZEH by Zeng et al, which can be delivered a maximum open-circuit voltage of 98.6 V and a short-circuit current of 0.3 µA with 9.8 µW instantaneous power.[24]

It is widely accepted that zinc oxide (ZnO) is one of the best piezoelectric materials for device fabrication owing to its superior piezoelectric, pyroelectric, biocompatibility, and easy synthesis method.[25] Therefore, several works have been done using ZnO as a filler in the PVDF matrix to fabricate piezoelectric NG.[26] But these NG devices have some limitations such as low output voltage

and low power density, poor economic performance, lack of durability, and so on. Thus, a new way to modify these difficulties has been done using different elements that incorporated ZnO nanoparticles as filler in the PVDF and its copolymer matrix like PVDF-hexafluoropropylene (PVDF-HFP). Modification of ZnO ceramic filler such as aspect ratio variation,[27] incorporation of third phase conductive filler[28] have already been investigated to enhance the NG output of PVDF-based composite system. The incorporation of group III elements in ZnO such as Al,[29] Ga,[30] In,[31] B[32] efficiently enhances the conductivity of the sample. Recently Zamiri et al have reported that Al-doped ZnO significantly enhanced the value of the dielectric constant of ZnO ceramics and the electrical conductivity in comparison to pure ZnO due to the increase of available charge carriers after substitution of Zn^{2+} ions by Al^{3+} ions.[33] Li et al also reported that a high dielectric constant value could be achieved by doping Al in ZnO sample at room temperature (30°C).[34] In light of this, it can be said that doping of Al^{3+} in ZnO nanoparticles may effectively improve the overall dielectric and ferroelectric properties of PVDF-HFP. Besides, it will be interesting to analyze the effect of Al^{3+} doping on the ZnO surface charge, which is a key factor behind the piezoelectric behavior of the nanocomposite. In spite of this, there are very few works have been reported on Al-doped ZnO using substrates other than the PVDF-HFP matrix. Tsai et al[35] reported that the average current, voltage, and power density of Al-doped ZnO piezoelectric harvester grown on ITO glass substrate are 0.76 µA, 1.35 mV, and 1.026 nW/mm², respectively. Whereas, Fang et al[36] reported on Al-doped ZnO NG grown on ITO glass substrate exhibiting the maximum voltage, current, and power density 60 mV, 0.7 µA, and 0.84 nW/mm², respectively. Also, Xue et al[37] reported that Ti substrate was grown Al-doped ZnO NG exhibited maximum ~1.6 V output voltage. Therefore, it will be quite fascinating to explore the effect of Al@ZnO nanofiller on the physicochemical as well as body motion-based energy harvesting properties of the nanocomposite. Here, PVDF-HFP instead of PVDF has been utilized as a matrix owing to its higher electromechanical coupling factor and high piezoelectric strain coefficient along with good mechanical properties, cost-effectiveness, chemical stability, weather resilient characteristics, and excellent film forming ability in comparison to the bare PVDF matrix.[38] Furthermore, external electrical poling is an important technique to enhance the NG output performance of the polymer-nanocomposites. The dipoles of the PVDF film were oriented along the field direction by the external electrical poling, which significantly enhances polarity, and leads to an increment of piezoelectricity.[39] The reorientation of the PVDF dipoles may enhance the dielectric

properties with low dielectric loss and decrease the leakage current value of the composite film which may have an impact on the energy storage capacity and energy generation performance of the devices.[39]

Here, we present a novel, low cost flexible PZEH comprised of wet chemically synthesized Al@ZnO nanorods incorporated PVDF-HFP composite. This Al@ZnO act as the nucleating agent, and significantly enhanced the dielectric, ferroelectric, and piezoelectric properties of the PVDF-HFP-based nanocomposite films. This fabricated energy harvester is capable of generating output voltage and power density of $\sim$26 V and 159.95 μW cm^{-2}, respectively. This device is also feasible for real-life applications as it is capable of charging a 2.2 μF capacitor up to 1.8 V and capable of lightning 30 LEDs connected in series. Thus, the fabricated NG may pave the way for the next-generation green energy source.

2 | EXPERIMENTAL

2.1 | Raw materials

Zinc nitrate hexahydrate [$Zn(NO_3)_2 \cdot 6H_2O$] (Sigma Aldrich), aluminum nitrate nonahydrate [$Al(NO_3)_2 \cdot 9H_2O$] (Sigma Aldrich), ethanol (C_2H_5OH) (Merck), sodium hydroxide [NaOH] (Merck), and distilled water were utilized to prepare Al-doped ZnO nanorods. PVDF-HFP [Molecular weight $\approx$400 000 g/mol, Sigma-Aldrich] and N,N-dimethylformamide (DMF) [$CH_3CON(CH_3)_2$] (Merck) were utilized to fabricate the nanocomposite films.

2.2 | Synthesis of pure ZnO and Al-doped ZnO nanorods

Pure ZnO nanorods as well as 5 wt% Al-doped ZnO ($Zn_{0.95}Al_{0.05}O$) nanorods were prepared by wet chemical synthesis procedure at ambient temperature. During this procedure, first of all, 2.974 g zinc nitrate hexahydrate was dissolved in distilled water and then 8 g sodium hydroxide was added to the mixed solution. For Al-doped ZnO synthesis, 0.235 g aluminum nitrate nonahydrate was added to the above-specified solution. After that, the mixed solution was continuously stirred for 1 h at room temperature (30°C). Thereafter pure ethanol was added to the resultant solution which kept for continuous stirring for 24 h. Finally, a precipitate was collected and centrifuged several times using distilled water and ethanol to eliminate any kind of impurities. The obtained product was white in color and it was dried (60°C) for further evaporation of any kind of solvent present.

2.3 | Fabrication of PVDF-HFP nanocomposites

The simple drop casting method was utilized to synthesize bare PVDF-HFP and other composite films. A series of composite films with different wt% was fabricated by dissolving PVDF-HFP pellets in DMF under constant stirring at 40°C. After complete dissolution of PVDF-HFP in DMF, the different weight percentage of wet chemically synthesized Al@ZnO powder (5 and 10 wt% powder with respect to PVDF-HFP) were added, individually. Thereafter, to obtain a homogeneous mixture, the solutions were continuously stirred for 24 h and sonicated for 1 h. After that, the polymer-composite films were fabricated by casting the resultant solution on a glass substrate and evaporated at 85°C for 4 h. Finally, at room temperature (30°C), the dried films were pulled off from the glass substrates to obtain self-standing composite films. The 5 and 10 wt% Al@ZnO/PVDF-HFP composite films were named 5PALZO and 10PALZO, respectively. Neat PVDF-HFP film was also prepared without any filler addition in the DMF solution. The thickness of the composite films as measured by a digital micrometer is 40 μm. 10PALZO composite film shows maximum polarity in the series. For further improvement of polarity, this composite film was poled at an electric field of 2.4 MV/cm for 2 h at 40°C. To fabricate the NG electrode-sample-electrode stack-like structure (using high purity silver paste as an electrode) with an active area of 6 cm^2 has been utilized. The entire fabrication procedure was shown in Figure 1. The detailed characterization techniques used for this work are presented in Discussion S1 of the Supporting Information (SI).

3 | RESULT AND DISCUSSION

3.1 | Characterization of filler particles

The structural properties of pure ZnO, as well as Al@ZnO nanorods, were investigated using x-ray diffractometer (XRD). Figure 2A presents the XRD patterns of ZnO and Al@ZnO nanorods.

The XRD pattern reveals the successful formation of ZnO rods (JCPDS card number #79-0205), with lattice parameters $a = b = 0.3248$ nm and $c = 0.5205$ nm, respectively. The absence of any additional peaks for Al@ZnO nanorods infers that the crystal structure remains invariant after doping. A more careful view of the enlarged image (Figure 2B) reveals a slight shifting of the peak position (100) toward a lower diffraction angle for the Al@ZnO nanorods. This shift in the 2θ position can be assigned to the introduction of Al^{3+} ion within
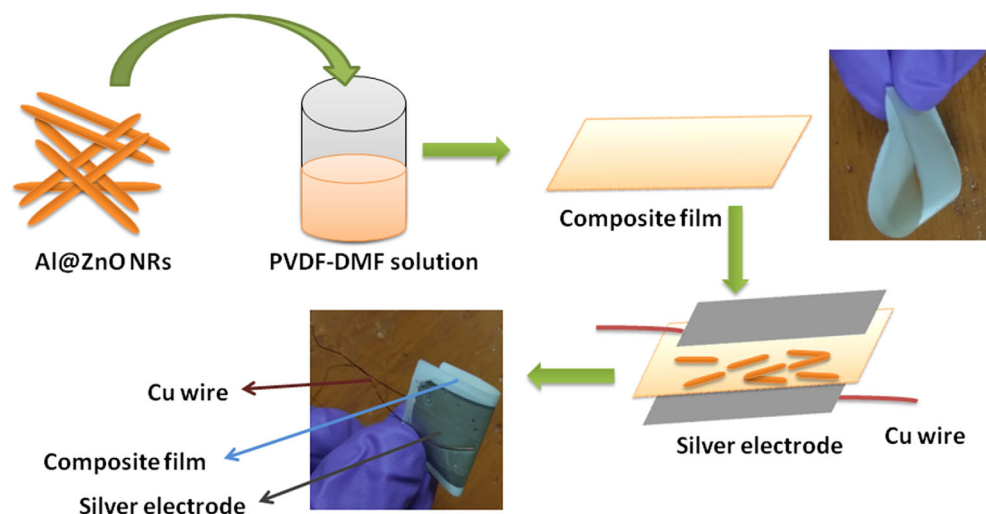
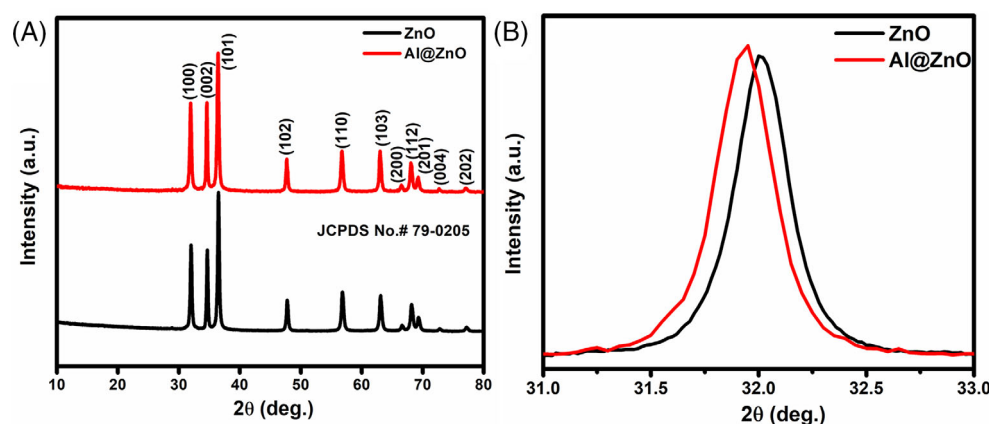**FIGURE 1** Schematic representation of the fabrication procedure of polymer-composite film

FIGURE 2 (A) XRD patterns of pure ZnO and Al@ZnO nanorods and (B) magnified view of (100) Bragg peak

the host ZnO lattice. To have a further detailed analysis, the crystallite size of ZnO and Al@ZnO nanorods were determined using Debye Scherrer's formula as follows:

$$D = \frac{0.9\lambda}{\beta\cos\theta} \quad (1)$$

where λ is the wavelength of the x-ray, β is the full width at half maxima of the XRD peaks, and θ is the Bragg's angle.[40] The crystallite size for pure ZnO and Al@ ZnO were found to be 32 and 24 nm, respectively, which implies a decrease in crystallite size after the incorporation of aluminum (Al^{3+}) ions in the ZnO host lattice. Reitveld refinement of XRD powder of ZnO and Al@ZnO nanorods was carried out using FullProf software (shown in Figure 3).

Refined parameters of pure ZnO and Al@ZnO samples were given in Table 1. The value of lattice parameter and volume of the unit cell was found to be decreased for Al@ZnO nanorods compared to pure ZnO nanorods. The reduction of lattice parameter, as well as cell volume value, can be attributed due to the smaller ionic radius of
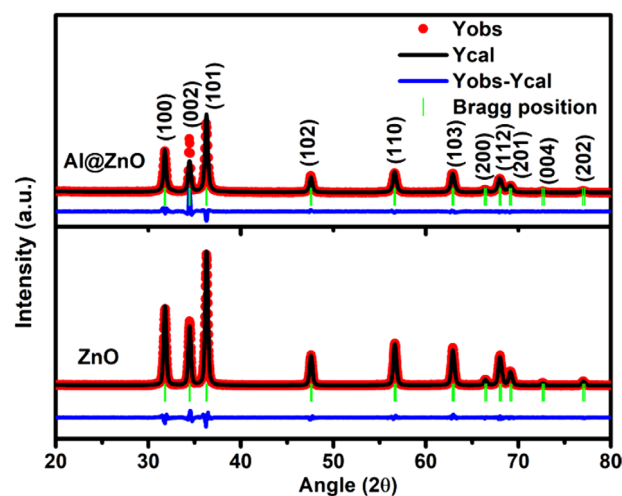

FIGURE 3 Reitveld refinement XRD patterns of pure ZnO and Al@ZnO nanorods

Al^{3+} ions than that of Zn^{2+} ions ($r_{Al}{}^{3+}$ = 0.63 Å, $r_{Zn}{}^{2+}$ = 0.74 Å).[41] This infers successful inclusion of Al^{3+} ion in the ZnO host lattice structure.

To analyze the effect of Al doping on the vibrational mode of ZnO nanorods, Raman, and Fourier-transform infrared spectroscopy (FTIR) spectroscopy of the sample was carried out. The successful incorporation of Al within ZnO can be further confirmed by Raman (Figure S1, Discussion S2), FTIR (Figure S2, Discussion S3), and leakage current density (Figure S3 with Discussion S4) of the Al@ZnO nanorods (Supporting Information).

To have a morphological analysis of the surface of pure ZnO and Al@ZnO nanorods field emission scanning electron microscopy (FESEM) technique was utilized (Figure 4A,B). The images reveal the formation of nanorods with pencil-like tip structures. Figure 4C,D demonstrates the size distribution of ZnO and Al@ZnO nanorods, respectively. Pure ZnO nanorods have an average diameter and length of ∼80 and ∼800 nm, respectively whereas Al@ZnO nanorods have an average diameter and length of ∼65 and ∼600 nm, respectively.

The typical transmission electron microscopy (TEM) of the prepared ZnO, as well as Al@ZnO nanorods, are depicted in Figure 5A,B, respectively, which indicated the formation of the uniform microstructure of the synthesized nanorods. The crystallinity of both nanorods was confirmed from the selected area electron diffraction (SAED) pattern. Further SAED patterns can be indexed to (100), (002), (110), and (102) planes of ZnO and Al@ZnO structures. SAED patterns are well matched with the XRD database and confirmed the crystallinity of both the nanorods. High-resolution TEM image (HRTEM) (Figure 5C,D, respectively) reveals that nanorods grow along the (100) direction.

Figure 6 represents energy-dispersive x-ray spectroscopy (EDS) spectra of Al@ZnO nanorods. The presence of Al with the elements Zn and O were confirmed from the EDS spectra. The use of carbon-coated Cu grid during TEM characterization resulted in extra peak Copper (Cu) and C which confirmed the purity of the synthesized samples. The atomic percentage of elements is given in the inset of Figure 6 which almost matched the doping percentage.
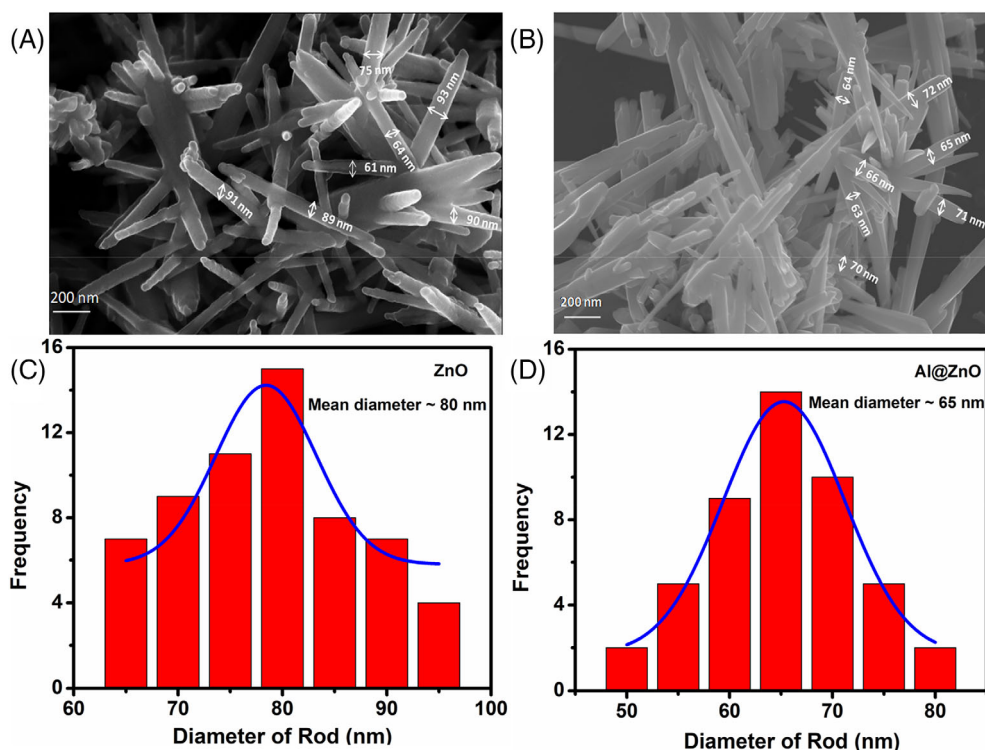
TABLE 1 Refined parameters from XRD data of pure ZnO and Al@ZnO

Parameters	Pure ZnO	Al@ZnO
Space group	P63mc	P63mc
Lattice parameter, $a = b$ (Å)	3.25070	3.24916
Lattice parameter, c (Å)	5.20620	5.20519
Cell angle $\alpha = \beta$ (°)	90	90
Cell angle γ (°)	120	120
Cell volume (Å^3)	47.643	47.5893
R_p, R_{wp}, and χ^2	8.00, 10.3, and 1.61	15.5, 16.9, and 2.13
S (goodness of fit) = R_{wp}/R_{exp}	1.27	1.45

FIGURE 4 FESEM images of (A) ZnO nanorods, (B) Al@ZnO nanorods; diameter distribution of (C) ZnO nanorods having mean diameter ∼80 nm, and (D)Al@ZnO nanorods having mean diameter ∼65 nm
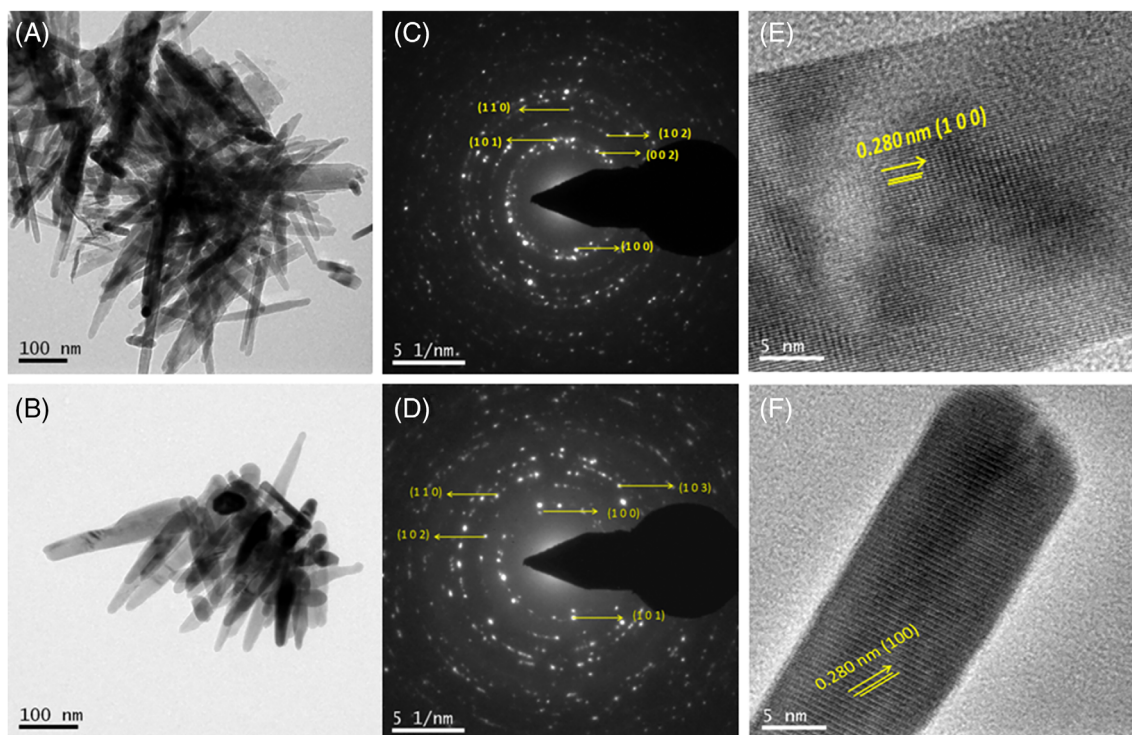
FIGURE 5 TEM images of (A) ZnO nanorods, (B) Al@ZnO nanorods, SAED pattern of (C) ZnO, (D)Al@ZnO nanorods, HRTEM images of (E) ZnO nanorods, and (F) Al@ZnO nanorods
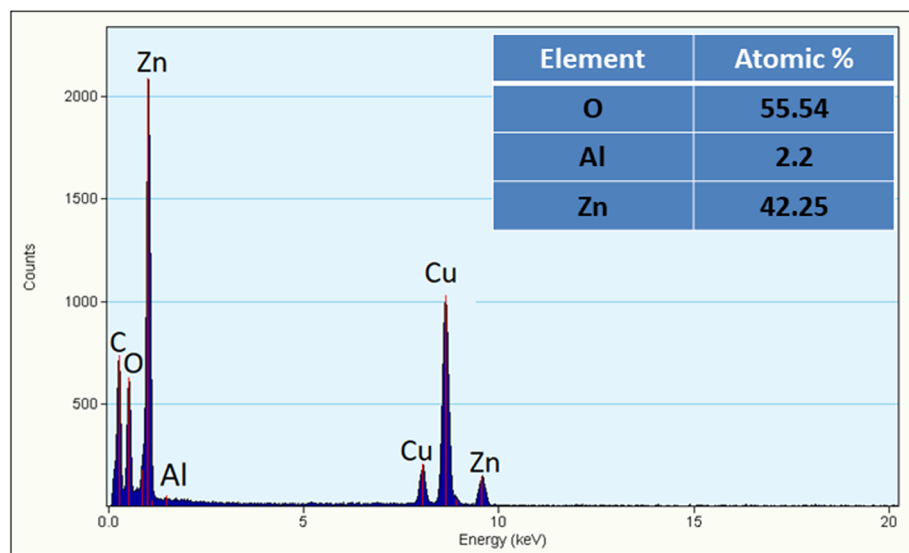

FIGURE 6 EDS spectra of Al@ZnO nanorods showing the presence of Al, inset shows the atomic percentage of Al

To determine the chemical state of undoped ZnO and Al@ZnO nanorods, XPS measurements were performed. Figure 7A presents the survey spectra of ZnO and Al@ZnO nanorods which revealed the existence of Zn, O, and Al elements in the synthesized samples. The core level of the Zn2p state was presented in Figure 7B where the peaks located at binding energy 1021.00 and 1044.23 eV attributed to $Zn2p_{3/2}$ and $Zn2p_{1/2}$ state, respectively.[42] For Al@ZnO nanorods, there is a peak shifting toward higher binding energies at 1021.7 and 1044.39 eV which corresponds to $Zn2p_{3/2}$ and $Zn2p_{1/2}$ state respectively, which is due to the addition of Al^{3+} into ZnO lattice.[43] The peak observed at ∼74.5 eV (shown in Figure 7C) is attributed to Al2p which confirmed the successful incorporation of Al^{3+} dopant in the ZnO host lattice. For better analysis, the core level XPS spectra of Al 2p level were fitted into two Gaussian curves, binding energy at a lower value of ∼74.2 eV is
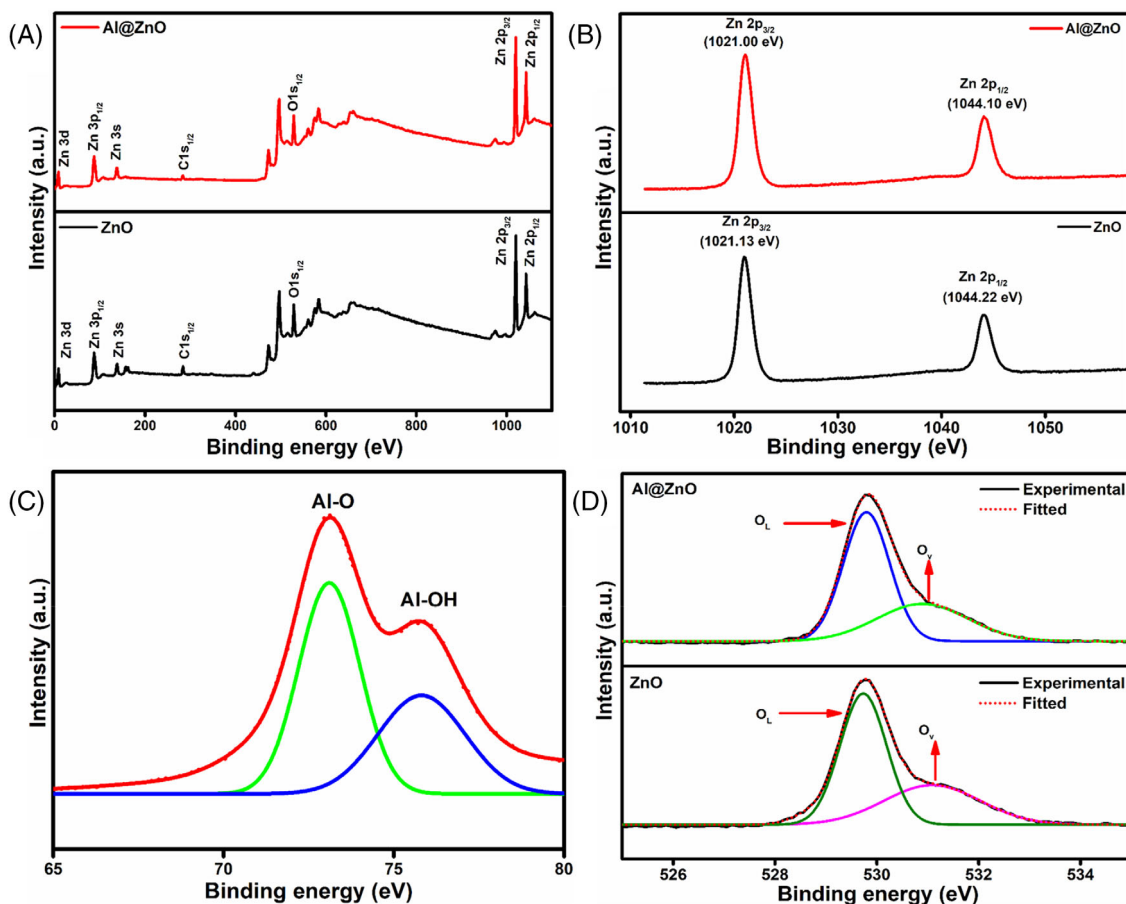
FIGURE 7 (A) XPS spectra, core level spectra of (B) Zn2p state, (C) deconvoluted Al 2p state, and (D) deconvoluted O1s state of ZnO and Al@ZnO nanorods

associated with Al-O bonds and binding energy at a higher value ~75.2 eV corresponds to Al-OH bonds,[43,44] which confirmed that the there is no metallic Al (binding energy ~72 eV) in the XPS spectra. No Al phases as observed from XRD and XPS studies conclude the successful addition of Al^{3+} ions into the host ZnO lattice.[43] Figure 7D represents the core level XPS spectra of O1s peaks for both ZnO and Al@ZnO nanorods. O1s spectra were fitted into two Gaussian components where binding energy at ~530.3 eV is assigned to O^{-2} ions in the ZnO lattice (O_L) and the binding energy at ~532.2 eV is attributed to O^{-2} ions in the oxygen-deficient region within ZnO structure which is associated with the concentration of oxygen vacancies or point defects (O_v).[43] There is a shifting of those two peaks toward higher binding energy at ~530.6 and 532.3 eV for Al@ZnO nanorods. The calculated area ratio (O_v/O_L) decreases for the Al@ZnO sample which reveals that there is a reduction of oxygen defects. This reduction of oxygen defects helps for the improvement of the electroactive phase within the nanocomposites.[45] Thereby, making the composite suitable for piezoelectric NG application.
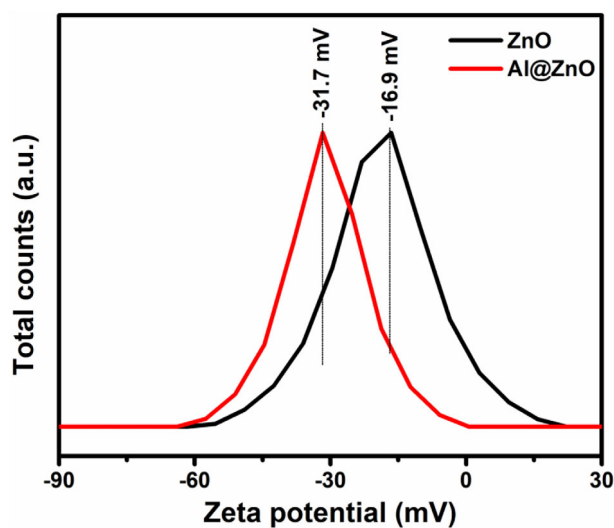

FIGURE 8 Zeta potential of ZnO and Al@ZnO nanorods

The surface charge of nanorod is also a key factor to better understand electrostatic interaction between PVDF-HFP chain and ceramic filler. For this purpose,
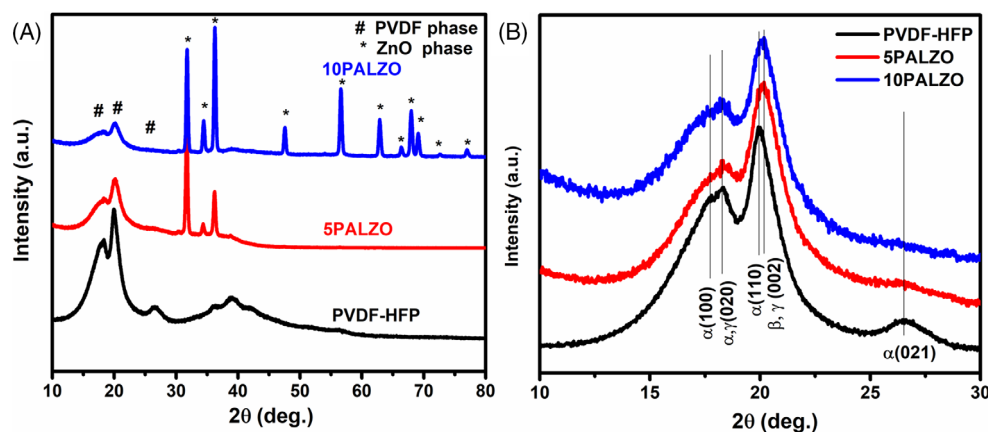
FIGURE 9 (A) XRD patterns of pure PVDF-HFP, 5PALZO, and 10PALZO composite films and (B)XRD patterns in the range of 10°-30°

zeta potential measurements of ZnO and Al@ZnO samples were carried out. The surface electrostatic charge of ZnO and Al@ZnO obtained from zeta potential analysis is depicted in Figure 8A. The Zeta potential value of ZnO and Al@ZnO were found to be −16.8 and −31.4 mV, respectively. The negative zeta potential value for both sample revealed that ZnO and Al@ZnO have a negative surface charge on their surfaces, which interact with –CH$_2$ dipole of PVDF-HFP through ion-dipole electrostatic interaction.[46] This interaction leads to the polar phase formation of the PVDF-HFP matrix. Thus, the nanofiller's surface acts as a nucleation center for the formation of the polar phase. A closer observation of Figure 8 reveals that the Al@ZnO reveals a higher amount of negative charge in comparison to ZnO nanorods. This higher amount of negative charge makes it a suitable candidate as a filler for the PVDF-HFP matrix.

3.2 | Characterization of Al@ZnO loaded PVDF-HFP composite films

The presence of the electro-active phase in polymer composites plays an important role in exhibiting good electrical properties of the composites.[16,28] As a consequence, XRD and FTIR characterization of the nanocomposites were carried out to investigate the presence of the electroactive phases in the respective samples (Figure 9A).

Pure PVDF-HFP exhibits a nonpolar α phase due to the TG$^+$TG$^-$ chain conformation of -CH$_2$−/–CF$_2$− dipoles of PVDF-HFP. With the incorporation of ceramic filler in the PVDF-HFP matrix, the dipoles reoriented themselves due to interfacial interaction between ceramic fillers and PVDF-HFP. As a result of nonpolar phase transformed into the polar β and γ phase due to TTTT and T$_3$G + T$_3$G-chain conformations. Figure 9B

demonstrates the dominance of polar phase fraction in the nanocomposites and 10PALZO is the most enriched one. XRD patterns of pure PVDF-HFP, 5PALZO, and 10PALZO composite films indicated that after mixing Al@ZnO nanorods in the PVDF-HFP matrix, PVDF-HFP retains their crystallinity. The comparison of XRD patterns of neat PVDF-HFP, 5PALZO, and 10PALZO composite film within the 2θ range from 10° to 30° is shown in Figure 9B. Pure PVDF-HFP exhibits a peak at 2θ ∼17.7°, 18.4°, 19.9°, and 26.6° corresponding to (100), (020), (110), and (021) planes, which is due to the presence of nonpolar α phase.[38] For the composite films, the intensity of the peaks at 17.7° and 26.6° decreased gradually with ceramic filler concentration and disappeared completely for 10 PALZO composite films. Besides, the main characteristics peak at 2θ–19.9° shifted toward higher diffraction angle gradually with filler concentration and maximum shifting was observed for 10PALZO composites film which indicates the phase transformation of PVDF-HFP from non-polar phase to polar phase.[28] To get a detailed idea of this phase transformation from non-polar to polar, the total degree of crystallinity and individual amount of beta crystallinity and gamma crystallinity of pure PVDF-HFP, 5PALZO, and 10PALZO films were calculated from deconvoluted XRD patterns of these samples (Figure S4).[28] The detailed calculation method and the obtained results are depicted in Discussion S5 of SI and Table S1 (SI).

To identify the quantitative crystalline phase in terms of local phonon bands of PVDF, FTIR characterization was carried out.

FTIR absorption spectra of pure PVDF-HFP, 5PALZO, 10PALZO, and 10 PALZO-P composite films are presented in Figure 10A (wavenumber region 1000–400 cm^{-1}). The figure reveals a significant enhancement of the polar phase within the composite film compared to bare PVDF-HFP. It was observed from FTIR spectra that there is a significant difference between PVDF-HFP and

FIGURE 10 (A) FTIR spectra of pure PVDF-HFP, 5PALZO, 10PALZO, and 10PALZO-P composite films, (B) variation of polar-phase with filler amount, (C) asymmetric and symmetric stretching vibration shift of composite film, and (D) damping coefficient evaluated from IR spectra of composite films
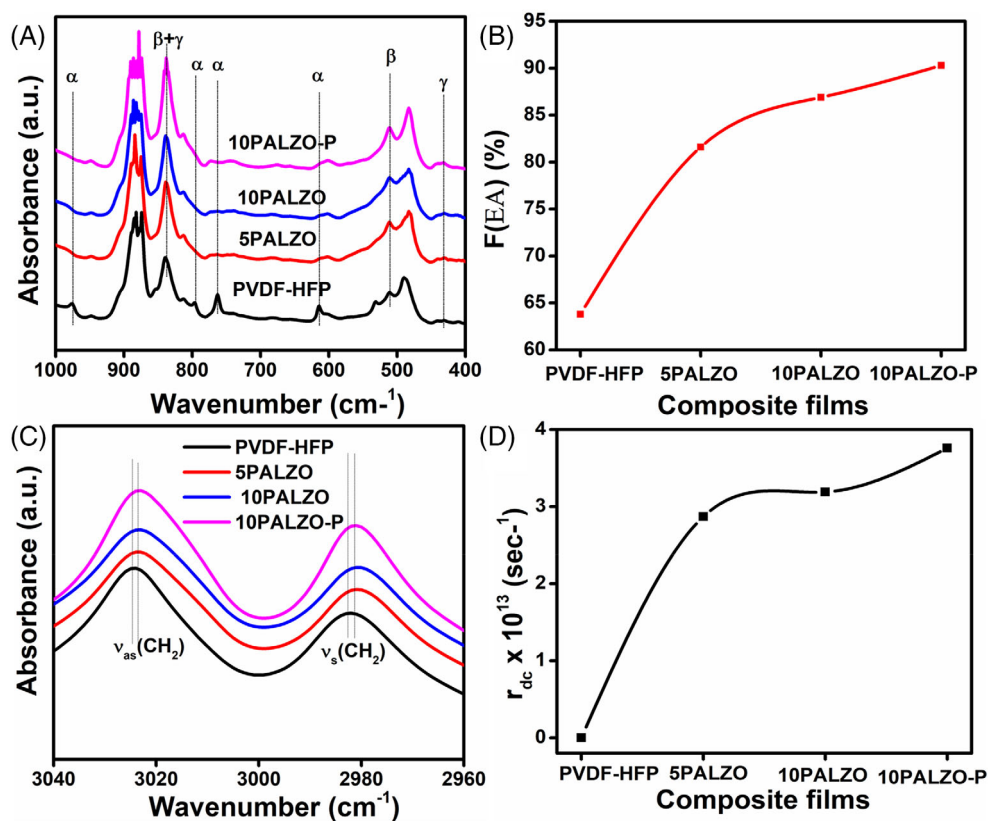
all composite films. FTIR spectra of pure PVDF-HFP show strong absorption peak at 409 and 488 cm^{-1} (CF$_2$ wagging), 532 cm^{-1} (CF$_2$ bending), 615 and 764 cm^{-1} (CF$_2$ bending and skeletal bending), and 796, 856, and 976 cm^{-1} (CH$_2$ rocking) which are attributed mainly to nonpolar α phase. FTIR spectra also reveal a weak absorption band of 431 cm^{-1} (correspond to polar γ phase), 510 cm^{-1} (CF$_2$ stretching associated with polar β phase), and 840 cm^{-1} (CF$_2$ stretching, CH$_2$ stretching and skeletal C-C stretching corresponds to polar β and γ phase).[5,29,39] The relative intensity of the peaks corresponding to the nonpolar α phase decreased gradually and some of the peaks disappeared completely with increasing filler concentration. A closure observation to Figure 10A shows that the relative intensity of the peaks at 510 and 840 cm^{-1} gradually increased with increasing filler concentration. Therefore polar phase of composite films increased in comparison with bare PVDF-HFP which clearly indicates the conversion of the PVDF-HFP phase from a nonpolar phase to a polar phase which also supports the XRD results. The quantitative amount of polar phase for each composite film as well as bare PVDF-HFP was calculated using the following equation

$$F(\text{EA}) = \frac{A_{\text{EA}}}{\left(\frac{K_{840}}{K_{764}}\right)A_{\text{NEA}} + A_{\text{EA}}} \quad (2)$$

where F(EA) presents the amount of electroactive phase fraction, A_{NEA} is the intensity of the absorbance bands at 764 cm^{-1}, and A_{EA} is the intensity of the absorbance bands at 840 cm^{-1}. $K_{840}(=7.7 \times 10^4$ cm^2 mol^{-1}) is the absorption coefficient at 840 cm^{-1} where $K_{764}(=6.1 \times 10^4$ cm^2 mol^{-1}) represents the absorption coefficient at 764 cm^{-1}, respectively.[45] The absorption bands at 840 cm^{-1} of bare PVDF-HFP, 5PALZO, 10PALZO, and 10PALZO-P nanocomposite films were deconvoluted (Figure S5 of SI) to determine the individual amounts of polar β and γ phases presence within them (Discussion S6 of SI) and the results are given in Table S2 of SI.[29]

The quantitative amount of β fraction indicates that (Figure 10B) 10PALZO posses' maximum amount of polar phase (86.9%) (much higher than bare PVDF-HFP 63.8%). The interfacial interaction between nanofillers and −CH$_2$− dipole of PVDF-HFP is responsible for such enhancement. To achieve a further increment in the polar phase fraction the sample with maximum polar phase (10PALZO) was kept under a constant electric field (2.4 MVcm^{-1}) for 2 h. As expected the applied electric field results in further alignment of CH$_2$ dipoles at the filler interface resulting in a further increment in the polar phase fraction (Figure 10B). To study the mechanism of interfacial interaction, FTIR spectra of all the samples were investigated within the wavenumber region
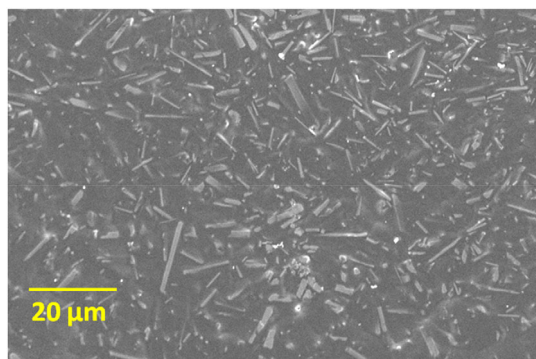
FIGURE 11 FESEM image of 10PALZO composite

3100 to 2900 cm^{-1} (Figure 10C), as this region was mainly assigned for asymmetric (ν_{as}) and symmetric (ν_s) stretching vibration band of –CH$_2$ dipole only, which are not coupled with any other vibrational modes.[39] A closer observation to Figure 10C indicates that, both symmetric and asymmetric stretching vibrational band of -CH$_2$ dipole of the composites shifts toward the lower wavenumber region in comparison with bare PVDF-HFP. The gradual shifting of these vibrational bands toward lower energy can be explained with the help of the damped harmonic oscillator model.[39] In light of the model initially it is being assumed that these two vibration bands have no damping for pure PVDF-HFP matrix. With the filler loading, electrostatic interaction occurs between the filler surface and the -CH$_2$ dipole of PVDF-HFP which will generate a source of damping. The interfacial interaction enhanced with increasing filler loading can be clearly seen with the enhanced damping coefficient (Figure 10D). The quantitative amount of electrostatic interaction of the composite films in terms of damping coefficient was calculated from the peak shifting of the asymmetric –CH$_2$ stretching vibrational band using the following equation.

$$r_{dc} = 4\pi C \left(\bar{\upsilon}_{PVDF}^2 - \bar{\upsilon}_{COMP}^2 \right)^{1/2} \qquad (3)$$

where r_{dc} represents the damping coefficient, c indicates the light velocity in free space, and the peak position associated with asymmetric –CH$_2$ stretching vibrational band of PVDF-HFP and composites are presented by $\bar{\upsilon}_{PVDF}$ and $\bar{\upsilon}_{COMP}$, respectively.[39] Figure 10D also reveals that the damping coefficient was maximum for 10PALZO-P composites confirming the maximum interfacial interaction.

To investigate surface morphology, the image of the 10PALZO sample is shown in Figure 11. FESEM image infers the nearly uniform dispersion of Al@ZnO nanorods within the PVDF-HFP matrix. Al@ZnO nanorods are well embedded in the PVDF-HFP matrix which confirmed the successful incorporation of Al@ZnO in the PVDF-HFP matrix.

Dielectric property is considered an important parameter for the development of energy storage devices.[47] As a consequence, the dielectric properties for all the composite films at ambient temperature (30°C) and pressure were carried out and shown in Figure 12A. Figure 12A represents an enhancement of the dielectric constant of all the composites than that of pure PVDF-HFP which can be assigned to the Maxwell-Wager-Siller interfacial polarization effect. The dielectric permittivity (at 1 kHz) increased from ∼8 for pure PVDF-HFP to ∼19 for 10PALZO composite film. The good dispersion of filler particles in the PVDF-HFP matrix is responsible for such enhancement. In the low-frequency region dielectric permittivity mainly increased due to the enhancement of space charge polarization with increasing filler loading in the PVDF-HFP matrix. Further, increased dielectric permittivity in the high-frequency region could be attributed due to the enhanced dipolar polarization. In this context, it is pertinent to be mentioned here that the dielectric constant for the composites has been increased with a considering low dielectric loss. In addition to that, the value of the dielectric loss is significantly small even less than 0.04 for the poled 10PALZO-P. Thus 10PALZO-P can be considered the best suitable candidate for energy harvesting as well as storing material. This reduction in the dielectric loss of 10PALZO-P after poling was mainly due to the lower leakage current due to dipole orientation along the field direction. The a.c. conductivity of the composite films was calculated using the following

$$\sigma = 2\pi f . \varepsilon_0 . \varepsilon_r^{''} \qquad (4)$$

where σ is the a.c. conductivity, f is the frequency, ε_0 is the free space permittivity, and $\varepsilon_r^{''}$ is the imaginary part of relative permittivity.[28] Frequency dependent a.c. conductivity of PVDF-HFP and all the composite films were represented in Figure 12C. The a.c. conductivity increased with increasing Al@ZnO concentration in PVDF-HFP which is due to the formation of a more conductive network in the polymer matrix with increased filler loading.

An efficient interfacial interaction leads to the enhancement of ferroelectric properties. In light of this, electric field-dependent electric displacement or polarization (D-E hysteresis loop or P-E loop) of pure PVDF-HFP, as well as composite films, were measured to investigate the ferroelectric properties of the composite films (at 1 Hz).

The room temperature D-E hysteresis loops of the pure PVDF-HFP, 5PALZO, 10PALZO, and 10PALZO-P

FIGURE 12 Frequency-dependent (A) dielectric permittivity, (B) dielectric loss, and (C) a.c. conductivity of PVDF-HFP, 5PALZO, 10PALZO, and 10PALZO-P nanocomposites
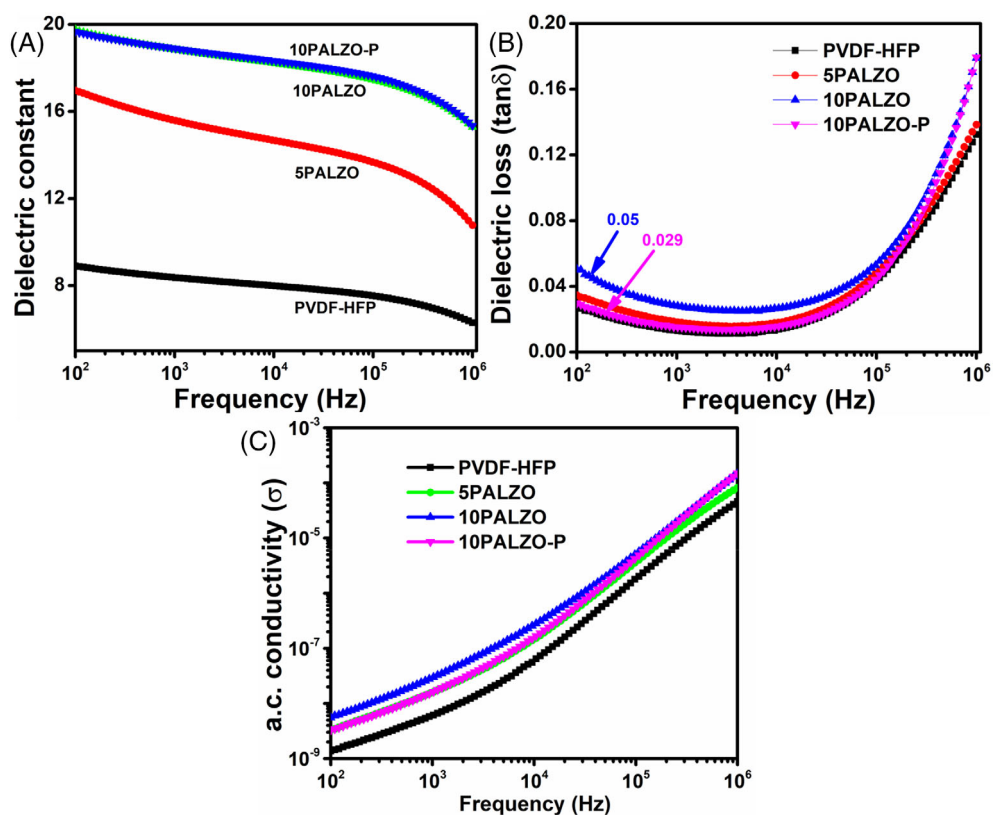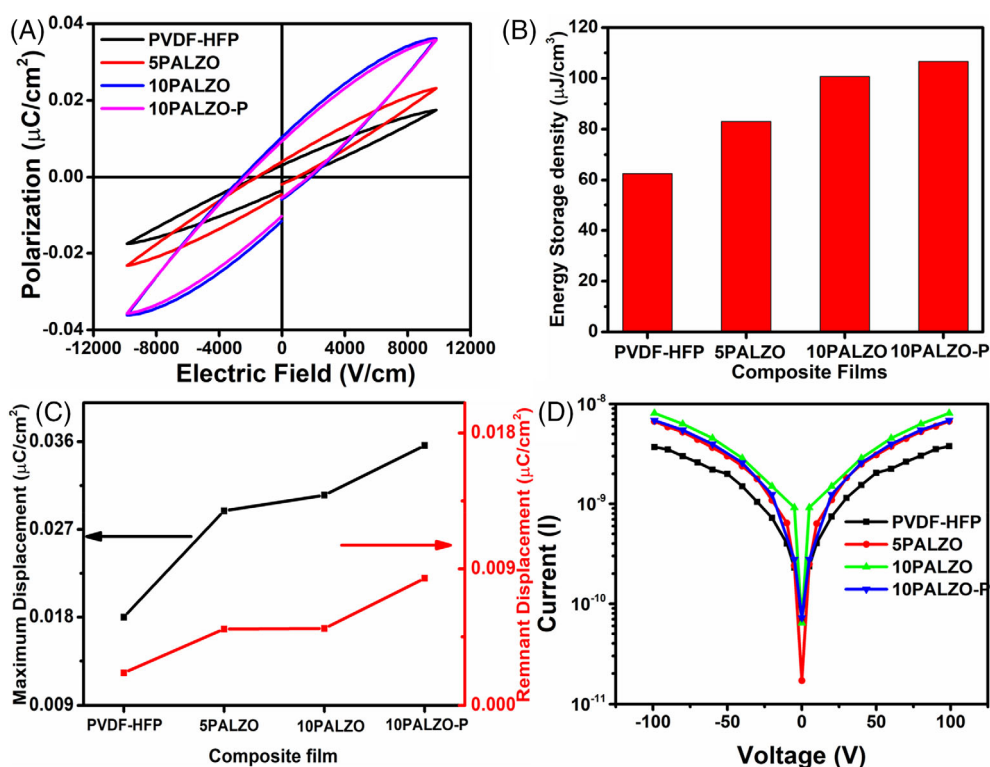
FIGURE 13 (A) Electric displacement vs applied electric field (D-E) loop, (B) variation of energy storage density, (C) variation of maximum displacement and remnant displacement of composite film, and (D) leakage current of PVDF-HFP, 5PALZO, 10PALZO, and 10PALZO-P nanocomposites, composite film

films were depicted in Figure 13A which indicates the presence of ferroelectric properties within the sample. Remnant electric displacement (D_r) and maximum

electric displacement (D_m) of all the samples (Figure 13C) were enhanced with increasing concentration of Al@ZnO in the polymer matrix. This result
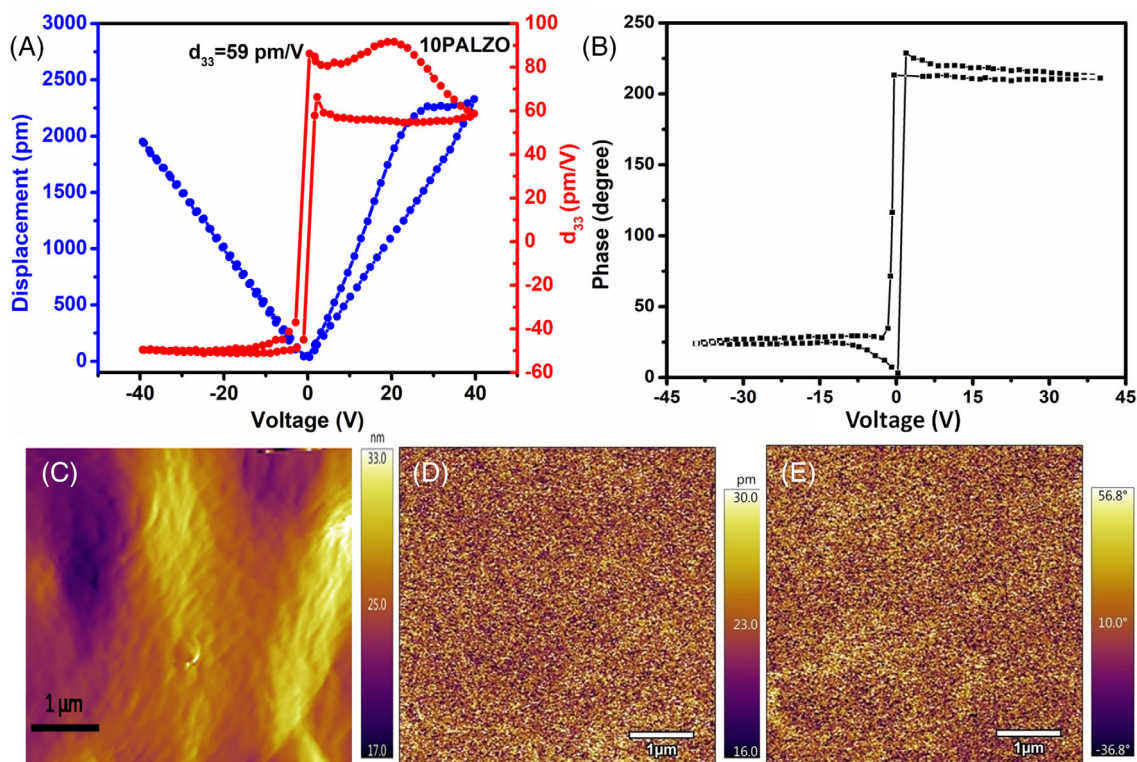
FIGURE 14 (A) Amplitude-voltage butterfly loop and d_{33}-V loop, (B) phase-voltage hysteresis loop, (C) topography image, (D) amplitude image, and (E) phase image of 10PALZO composite film

confirmed the enhancement of ferroelectric properties of the composites with a significant small leakage current (Figure 13D). This enhancement of ferroelectric properties was due to the strong interfacial interaction between the PVDF-HFP matrix and Al@ZnO filler. The increased interfacial interaction between the PVDF matrix and filler leads to an enhancement of the polar phase within the composites, which increases the ferroelectric property.

In general, the energy density (U) of a non-linear dielectric material is given by U = ∫ EdD, where E and D denote the electric field and displacement, respectively.[45] Different portions of the D-E loops were integrated to calculate the energy storage and loss density. The energy storage density (U_{stored}) of the nanocomposites was calculated using

$$U_{stored} = \int_{D_r}^{D_m} EdD \qquad (5)$$

An increment in the stored energy density for the loaded samples can be seen in Figure 13B. However, it should be mentioned here that the maximum energy density ∼111.2 μJcm^{-3} is obtained from the poled 10PALZO-P sample, implying the best suitable candidate for energy

storage material. Poling process helped to reorient the dipoles along the field direction which increased the polar phase formation.[39] The breakdown voltage of the device was measured through a P-E loop by applying different voltages (shown in Figure S6 of SI). The polarization value of the nanocomposite increased with an increasing applied electric field. The breakdown strength of the nanocomposite was 1120 kVcm^{-1}. The leakage current of the pure PVDF-HFP, 5PALZO, 10PALZO, and poled 10PALZO-P samples are presented in Figure 13D, respectively. The reduction of the leakage current value of the 10PALZO-P film (Figure 13D) after poling was mainly due to the dipole orientation of the composite.[39] This low leakage current also shows the applicability of the poled sample for a good NG.

To investigate the local piezoelectric properties and ferroelectric domain switching behavior of the composite film after Al doping within ZnO, piezo force microscopy (PFM) measurement of the unpoled 10PALZO sample was carried out.[5,48] In this measurement, a Ti/Ir coated conductive tip has been used with an AC voltage in the range of 1 to 2 V. The sweeping dc bias voltage applied to the samples was in the range of ±60 V (PVDF-HFP) and ±40 V (10PZO and 10PALZO), respectively. Figure 14A,B represents the piezoresponse loop and phase hysteresis loop of the 10PALZO sample under an applied DC bias
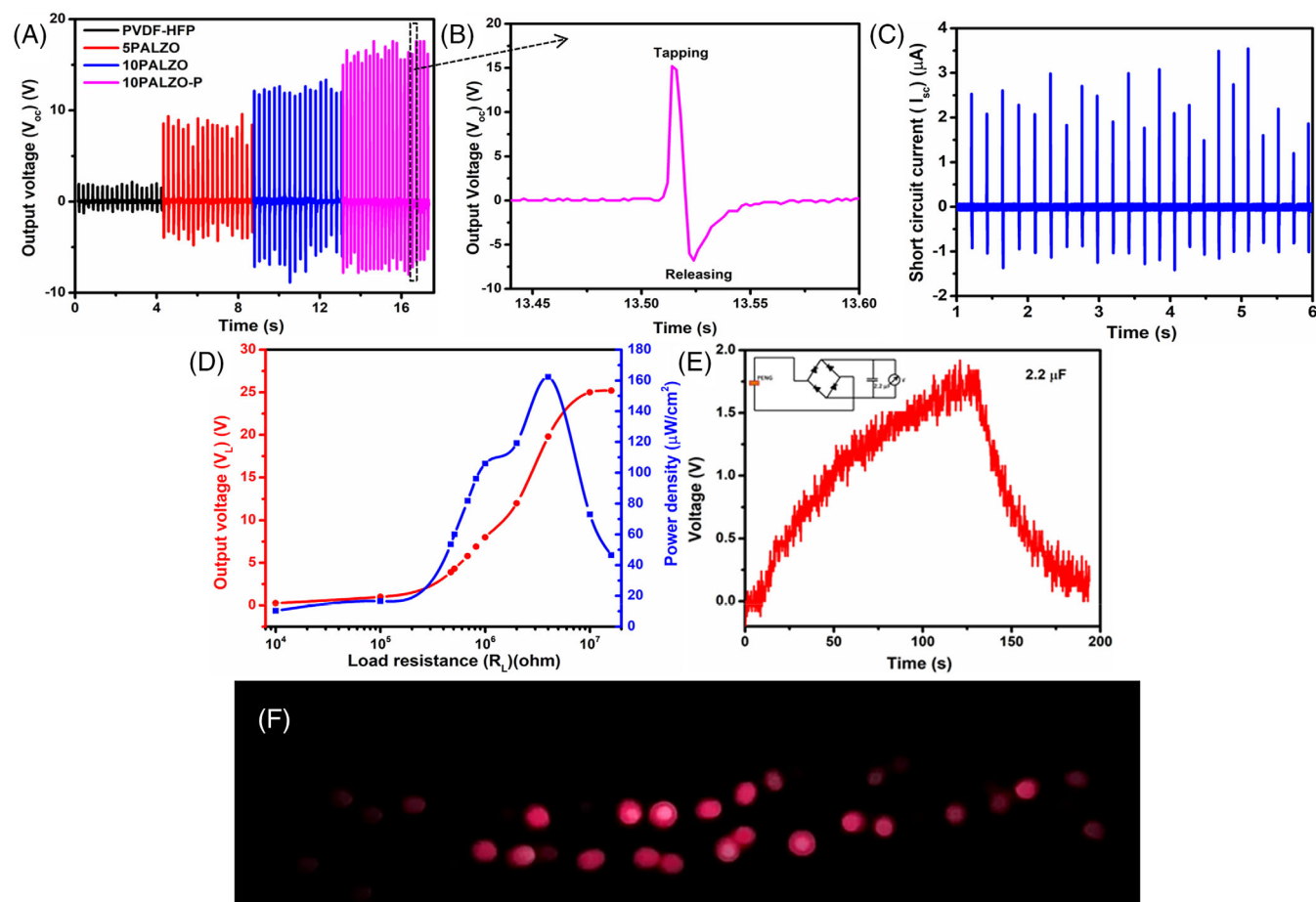
FIGURE 15 (A) Open circuit output voltage of PVDF-HFP, 5PALZO, 10PALZO, and 10PALZO-P nanocomposites, (B) magnified image of one cycle of a 10PALZO-P film, (C) short circuit output current of 10PALZO-P film, (D) the variation of output voltage and power density with load resistance, (E) capacitor charging and discharging graph, and (F) LED glowing performance of the 10PALZO-P composite film

voltage ±40 V, respectively. Phase-hysteresis loop shows (Figure 14B) the 180° phase difference which proves that the dipoles are easily capable of being switched upward or downward direction under an applied electric field which confirms the existence of ferroelectric domain switching behavior in the composite film.[5,48] The asymmetric behavior of the loop arises due to the generated internal bias within composite film.[48] 10PALZO composite contains a significant amount of β phase due to the TTTT trans conformation of $-CH_2/-CF_2$ dipole of PVDF-HFP. With the application of dc-bias across 10PALZO film, electric dipoles are rotated around the carbon backbone generating ferroelectricity within it which is confirmed by the ferroelectric switching behavior of the phase-voltage hysteresis loop.[5] Since the piezoelectric coefficient (d_{33}) is directly proportional to the electromechanical response of the material, the d_{33}-voltage loops can be indirectly derived from the amplitude-voltage butterfly loop using the modified equation of converse piezoelectric effect $d_{33} = D\text{-}D_1/V\text{-}V_1$, where D_1 is the piezoelectric displacement and V_1 is the applied voltage

at the intersection.[49] Figure 14A represents the d_{33}-V loops of pure 10PALZO composite films. d_{33}-V loops of pure PVDF-HFP and ZnO incorporated PVDF-HFP (10PZO) are shown in Figure S9 of SI. The calculated piezoelectric coefficient as obtained from Figure 14A and Figure S9 was ~15, 21, and 59 PM/V for pure PVDF-HFP, 10PZO, and 10PALZO, respectively. The result infers that the incorporation of ZnO nanorods within the PVDF-HFP matrix cannot enhance the piezoelectric coefficient significantly. Interestingly, after the addition of Al@ZnO filler within the matrix, the piezoelectric coefficient enhanced drastically to ~59 pm/V which is much higher than that of pure PVDF-HFP. This increment of piezoelectric coefficient with the addition of Al@ZnO filler was mainly attributed to the increased polar phase fraction as obtained by FTIR results (Figure 10). Figure 14C–E represents the topography, amplitude, and phase images of 10PALZO composite film, respectively. PFM amplitude is associated with the local piezoelectric coefficient due to electromechanical coupling where the orientation of domains or polarization can be reflected by

TABLE 2 Comparison of piezoelectric output voltage and power with other reported polymer-based nanogenerator

| Si. No.	Name of the material	Input source	Output voltage	Power density	Ref. no
1.	BT@PVDF−TrFE	Tapping force 100 N, 2.5 Hz	59.5 V	165.8 μW	20
2.	$CsPbI_3$/PVDF	Force 2.7 N, 30 Hz	26 V	25 μW	21
3.	PVDF-0.67($BiFeO_3$)-0.33($BaTiO_3$)	Pressure 1 kgf, 3 Hz	83 V	142 mW/m^2	22
4.	PVDF–$ZnSnO_3$-MoS_2	Pressure 1 kgf, 3 Hz	26 V	28.9 mW/m^2	23
5.	Ga-$PbZr_xTi_{1-x}O_3$ (PZT)@GaO_x/PVDF-TrFe	Force 12 N, 30 Hz	98.6 V	9.8 μW	24
6.	Co-doped ZnO/PVDF-HFP	Vibrating shaker	2.8 V	-	40
7.	Ba-doped $BiFeO_3$/PVDF	Finger tapping	20 V	318 μW	45
8.	ZnO NWs/PVDF	Bending tester	~6.9 V	6.624 μW	50
9.	$BaTiO_3$ nanoparticles and graphitic carbon/PDMS	Bending Stage	3.2 V	-	51
10.	BCTZ nanoparticles-polymer composite	Bending	15 V	8 μW	52
11.	MoS_2/PVDF	27.5 N	84 V	47 mW/cm^3	53
12.	PVDF-KNN	Finger tapping	3.7 V	-	54
13.	$ZnTiO_3$-PVDF	Finger tapping	25.5 V	8.22 μW/cm2	55
14.	$KNbO_3$ nanowires	Bending tester	10.5 V	4.5 μW	56
15.	ZnO-PVDF	Hitting by a cylinder of diameter 1 cm	3 V	0.21 μW/cm^2	57
16	Methylammonium lead iodide ($CH_3NH_3PbI_3$)/PVDF	Human finger tapping	1.6 V	2.5 μW/cm2	58
17.	D-phe@ZnO/P(VDF-TrFE)	Periodic pressure (10 N, 2 Hz)	~33 V	8.5 μW/cm^2	59
18.	KNN/ZnO/PVDF	Finger tapping	~ 25 V	11.31 μW/cm^2	60
19.	PZT/PDMS	Force 113 N	176 V	177 μW/cm^2	61
20.	PDMS/Li:ZnO/Ti3C2	Bending	~10 V	9 μW/cm^2	62
21.	Al-doped ZnO-PVDF/HFP	Finger tapping	26 V	159.95 μW cm^{-2}	This work
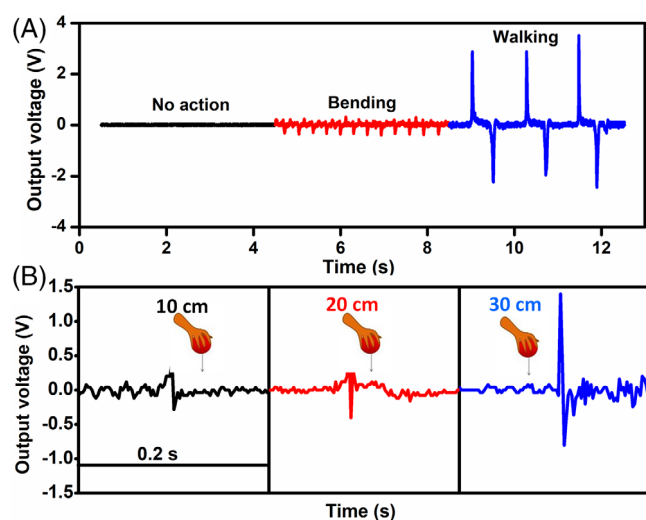
FIGURE 16 (A) Variation of output voltage with different human body activities and (B) output voltage variation for the ball dropping from 10, 20, and 30 cm heights

the phase.[5,48] Domains with opposite polarization can be distinguished by image contrasts (shown in Figure 14D). The dark brown and bright yellow regions are mainly attributed to the polarization of domains with upward and downward directions, respectively. Both amplitude and phase images with different contrasts confirmed the presence of piezoelectric and ferroelectric properties within the composite film.[48] PFM results confirmed that the 10PALZO composite film possesses good ferroelectric and piezoelectric properties, making it suitable for good mechanical energy harvesting.[5]

To investigate the efficiency of the sample as an efficient energy harvesting device (PZEH) the voltage generation capacity of the fabricated composite films, under compressing and releasing process of finger imparting on them were observed (pressure ~4 kPa and frequency ~5 Hz).

The open circuit output voltage as obtained from pure PVDF-HFP and composite films is illustrated in

Figure 15A. It can be clearly seen from the figure that with the increasing filler loading, the open circuit output voltage of the nanocomposite films increased gradually and reaches a maximum value of ∼22 V for 10 wt% of Al@ZnO loading. When mechanical force was applied, the permanent dipoles oscillated and as a result of this oscillation, an electric potential difference generated between the top and bottom electrodes. This potential allows the free electrons to circulate across an external circuit, resulting in the generation of electric signals.[39,56] Therefore, the increased value of output voltage with filler loading was due to the enhanced polarity of the system. A careful observation of the figure indicates that the output voltage of 10PALZO-P film further increased to ∼26 from 22 V which was mainly attributed to the highest polar phase formation within the system generated by reorientation of polymer chains due to poling.[39] To confirm the piezoelectric voltage of the device, the switching polarity test of this composite was done by reversing the electrode connection. Nearby same voltage was obtained after reversing the electrode connection (shown in Figure S7) which proved that the output voltage arises from the piezoelectric effect.[28] Again, the cross-sectional FESEM image of the device as presented in Figure S8 of SI also confirms the piezoelectric nature of the device as no such spacing has been observed between the electrode and the functional layer.[5] Thus, the electric signals are purely piezoelectric. The enlarged image of one output pulse, undercompressing, and releasing processes of finger tapping was presented in Figure 15B. Figure 15C reveals the generated short circuit current (4 μA) from the device using 10 wt% Al@ZnO incorporated PVDF-HFP under the action of finger imparting (force 4 kPa and frequency ∼5 Hz).The obtained a.c. output voltage was rectified to d.c. voltage using a bridge rectifier (DB107) which was capable of charging a 2.2 μF capacitor up to ∼1.8 V (shown in Figure 15E). The fabricated PZEH is also capable of illuminating instantly 30 commercial LEDS under repeated finger imparting connected in series (Figure 15F) (lightening of LEDs by finger imparting was shown in video S1). To examine the real-life feasibility of the fabricated device, power density was calculated using the formula given below.

$$P = \frac{1}{A}\frac{V_L^2}{R_L} \qquad (6)$$

where V_L is the output voltage through the load resistance (R_L) and A is the area of the composite film. The obtained output voltage and power density of 10PALZO-P composite film with different load resistance were presented in Figure 15D. The output voltage increased gradually with increasing load resistance and reached a maximum value of 26 V across an 8 MΩ load resistance. The maximum output power density of the 10PALZO-P composite film was found to be 159.95 μWcm^{-2} at 8 MΩ load resistance. The maximum power density, as well as generated voltage as obtained from PZEH, is quite higher than the other previously reported PVDF-based NG (Table 2). In this context, it is pertinent to be mentioned here that the output performance of the fabricated PZEH is quite comparable with other doped ZnO filler-loaded matrixes (Table S3).

Further, for real-life application, the sensitivity of the 10PALZO-P film was also checked by applying different types of human body motion. As shown in Figure 16A, a output voltage of ∼2 V was generated for bending of the device while for walking the output voltage was ∼4.5 V. This result indicated that the device showed sensitivity for different types of human body motions. Therefore, this composite can be used as physical activity sensor for detecting body motions or activities. To check the pressure sensitivity of the 10PALZO-P sample, a rubber ball of mass 20 g was dropped from 10, 20, and 30 cm heights, and the corresponding output signals was recorded respectively, which was shown in Figure 16B. Output voltage improved with increasing height of ball dropping which was due to the enhancement of pressure. The output voltage variation with applied pressure was depicted in Figure S10 with Discussion S7 of SI. This result clearly indicates that the fabricated device has high sensitivity and this may be used as a height monitoring sensor too.[38]

4 | CONCLUSION

In summary, it can be concluded that Al@ZnO incorporated PVDF-HFP films were successfully developed using the simple and cost-effective solvent casting technique. An increment in electroactive polar phase fraction was found with the increasing loading of Al@ZnO. An effective interfacial interaction between filler and the polymer matrix results in maximum electroactive phase fraction ($F(EA) > 85\%$) β for 10 wt% Al@ZnO loaded PVDF-HFP composite. Moreover, a more than two times increase in dielectric constant (∼19) was achieved in comparison to bare PVDF-HFP (∼8). In addition to that, 10PALZO nanocomposite exhibited a good energy storage density of 94.1 μJ/cm^3. The fabricated piezoelectric energy harvesting device using optimized 10PALZO nanocomposites was able to deliver an open circuit output voltage of ∼22 V under gentle human finger tapping (frequency 4 Hz and pressure ∼4 kPa). A further enhancement in the electrical performance of 10PALZO nanocomposite was achieved by applying a high electric field (2.4 MVcm^{-1}). Applied electric field results in further

alignment of polymer chains leading toward an electroactive phase fraction as high as ~91.2%. Though the dielectric constant has been increased slightly after poling there is a considerable low dielectric loss (0.03). Owing, to such electrical properties, poled 10PALZO nanocomposite exhibited a good energy storage density of 111.2 μJcm^{-3} (at 1 Hz). A further increment in open circuit output voltage to 26 V was obtained from a 10PALZO-P nanocomposite-based energy harvester under similar imparting conditions. A high instantaneous power density of 159.95 μWcm^{-2} and short circuit current of ~4 µA, enables the NG to be used in real-life applications such as fast charging of capacitors (2.2 µF up to 1.8 V), energy generation from human body motion, and powering a panel of commercial LEDs. Furthermore, the piezoelectric NG has been used efficiently as a height-monitoring sensor. Thereby, the fabricated flexible piezoelectric NG can effectively pave the way toward low-cost, flexible as well as wearable piezoelectric energy harvesting devices.

CONFLICT OF INTEREST

There are no conflicts of interest.

DATA AVAILABILITY STATEMENT

The raw/processed data required to reproduce these findings cannot be shared at this time as the data also forms part of an ongoing study.

REFERENCES

1. Kar E, Barman M, Das S, et al. Chicken feather fiber-based bio-piezoelectric energy harvester: an efficient green energy source for flexible electronics. *Sustainable Energy Fuels*. 2021;90:1857-1866.
2. Yang Y, Guo W, Pradel KC, et al. Pyroelectric Nanogenerators for harvesting thermoelectric energy. *Nano Lett*. 2012;12:2833-2838.
3. Raj NP, Abisegapriyan KS, Khandelwal G, Alluri NR, Kim SJ. Lead-free ferroelectric $Bi_{0.5}Na_{0.5}TiO_3$ based flexible, lightweight Nanogenerator for motion monitoring application. *Sustainable Energy Fuel*. 2020;4:5636-5644.
4. Roundy S, Takahashi E. A planar electromagnetic energy harvesting transducer using A multi-pole magnetic plate. *Sens Actuators A*. 2013;195:98-104.
5. Kar E, Bose N, Dutta B, Mukherjee N, Mukherjee S. $MWCNT@SiO_2$ heterogeneous Nanofiller-based polymer composites: A single key to the high-performance piezoelectric Nanogenerator and X-band microwave shield. *ACS Appl Nano Mater*. 2013;7:10424.
6. Ding R, Liu H, Zhang X, et al. Flexible piezoelectric nanocomposite generators based on Formamidinium Lead halide perovskite nanoparticles. *Adv Funct Mater*. 2016;26:7708-7716.
7. Ding R, Zhang X, Chen G, et al. High-performance piezoelectric Nanogenerators composed of Formamidinium Lead halide perovskite nanoparticles and poly (vinylidene fluoride). *Nano Energy*. 2017;37:126-135.
8. Orrego S, Shoele K, Ruas A, et al. Harvesting ambient wind energy with an inverted piezoelectric flag. *Appl Energy*. 2017; 194:212-222.
9. Karan SK, Bera R, Paria S, et al. An approach to design highly durable piezoelectric Nanogenerator based on self-poled PVDF/AlO-rGO flexible nanocomposite with high power density and energy conversion efficiency. *Adv Energy Mater*. 2016; 6:1601016.
10. Sudo T, Sasaki H, Masuda N, Drewniak JL. Electromagnetic interference (EMI) of system-on-package (SOP). *IEEE Trans Adv Packag*. 2004;27:304-314.
11. Lovinger AJ. Ferroelectric polymers. *Science*. 1983;220:1115-1121.
12. Fukada E. History and recent Progress in piezoelectric polymers. *IEEE Trans Ultrason Ferroelectr Freq Control*. 2000;47: 1277-1290.
13. He F, Fan J, Lau S. Mechanical, and dielectric properties of graphite reinforced poly (Vinylidene fluoride) composites. *Polym Test*. 2008;27:964-970.
14. Lin ZH, Yang Y, Wu JM, Liu Y, Zhang F, Wang ZL. $BaTiO_3$ nanotubes-based flexible and transparent Nanogenerators. *J Phys Chem Lett*. 2012;3:3599-3604.
15. Soin N, Zhao P, Prashanthi K, et al. High performance triboelectric Nanogenerators based on phase-inversion piezoelectric membranes of poly(Vinylidene fluoride)-zinc Stannate (PVDF-$ZnSnO_3$) and Polyamide-6 (PA6). *Nano Energy*. 2016;30: 470-480.
16. Karan SK, Mandal D, Khatua BB. Self-powered flexible Fe-doped RGO/PVDF nanocomposite: an excellent material for A piezoelectric energy harvester. *Nanoscale*. 2015;7:10655-10666.
17. Wankhade SH, Tiwari S, Gaur A, Maiti P. PVDF–PZT nanohybrid based nanogenerator for energy harvesting applications. *Energy Rep*. 2020;6:358-364.
18. Garain S, Jana S, Sinha TK, Mandal D. Design of in situ poled Ce^{3+}-doped electrospun PVDF/graphene composite nanofibers for fabrication of Nanopressure sensor and ultrasensitive acoustic Nanogenerator. *ACS Appl Mater Interfaces*. 2016;8: 4532-4540.
19. Sinha TK, Ghosh SK, Maiti R, et al. Graphene-silver-induced self-polarized PVDFBased flexible Plasmonic Nanogenerator toward the realization for new class of self powered optical sensor. *ACS Appl Mater Interfaces*. 2016;8:14986-14993.
20. Cho Y, Jeong J, Choi M, et al. $BaTiO_3$@ PVDF-TrFE nanocomposites with efficient orientation prepared via phase separation nano-coating method for piezoelectric performance improvement and application to 3D-PENG. *Chem Eng J*. 2022;427: 131030.

21. Zhu W, Khan AA, Rana MM, et al. Poly(vinylidene fluoride)-stabilized black γ-phase $CsPbI_3$ perovskite for high-performance piezoelectric Nanogenerators. *ACS Omega*. 2022; 7:10559-10567.

22. Muduli SP, Veeralingam S, Badhulika S. Multilayered piezo-electric Nanogenerator based on Lead-free poly(vinylidene fluoride)—$(0.67BiFeO_3–0.33BaTiO_3)$ electrospun nanofiber Mats for fast charging of Supercapacitors. *ACS Appl Energy Mater*. 2022;5(3):2993-3003.

23. Muduli SP, Veeralingam S, Badhulika S. Interface induced high-performance piezoelectric Nanogenerator based on a electrospun three-phase composite nanofiber for wearable applications. *ACS Appl Energy Mater*. 2021;4(11):12593-12603.

24. Zeng S, Zhang M, Jiang L, et al. Wearable Piezoelectric Nano-generators Based on Core–Shell Ga-PZT@GaO_x Nanorod-Enabled P(VDF-TrFE) Composites. *ACS Appl Mater Interfaces*. 2022;14(6):7990-8000.

25. Wang ZL, Song J. Piezoelectric nanogenerators based on zinc oxide nanowire arrays. *Science*. 2006;312:242-246.

26. Choi M, Murillo G, Hwang S, et al. Mechanical and electrical characterization of PVDF-ZnO hybrid structure for application to nanogenerator. *Nano Energy*. 2017;33:462-468.

27. Pratihar S, Medda SK, Sen S, Devi PS. Tailored piezoelectric performance of self-polarized PVDF-ZnO composites by optimization of aspect ratio of ZnO nanorods. *Polym Compos*. 2020; 41:3351-3363.

28. Pratihar S, Patra A, Sasmal A, Medda SK, Sen S. Enhanced dielectric, ferroelectric, energy storage and mechanical energy harvesting performance of ZnO–PVDF composites induced by MWCNTs as an additive third phase. *Soft Matter*. 2021;17:8483-8495.

29. Minami T, Nanto H, Takata S. Substrate temperature dependence of transparent conducting Al-doped ZnO thin films prepared by magnetron sputtering. *Japan J Appl Phys*. 1984; 23:280.

30. Wang H, Baek SH, Song JJ, Lee JH, Lim SW. Microstructural and optical characteristics of solution-grown Ga-doped ZnO nanorod arrays. *Nanotechnology*. 2008;19:075607.

31. Jung MN, Koo JE, Oh SJ, et al. Influence of growth mode on the structural, optical, and electrical properties of in-doped ZnO nanorods. *Appl Phys Lett*. 2009;04:041906.

32. Vijayakumar PS, Blaker KA, Weiting RD, Wong B, Halani AT, Park C. US Patent. 1988;4:149.

33. Zamiri R, Singh B, Belsley MS, Ferreira JMF. Structural and dielectric properties of Al-doped ZnO nanostructures. *Ceramic Int*. 2014;40:6031-6066.

34. Li X, Cao X, Xu L, et al. High dielectric constant in Al-doped ZnO ceramics using high-pressure treated powders. *J Alloys Compd*. 2016;657:90-94.

35. Chang W-Y, Fang T-H, Tsai J-H. Electromechanical and photo-luminescence properties of Al-doped ZnO Nanorods applied in piezoelectric Nanogenerators. *J Low Temp Phys*. 2015;178: 174-187.

36. Fang T-H, Kang S-H. Physical properties of ZnO:Al nanorods for piezoelectric nanogenerator application. *Current Nanosci*. 2010;6:505-551.

37. Zang W, Wang W, Zhu D, Xing L, Xue X. Humidity-dependent piezoelectric output of Al–ZnO nanowire nanogenerator and its applications as a self-powered active humidity sensor. *RSC Adv*. 2014;4:56211-56215.

38. Chinya I, Pal A, Sen S. Flexible, hybrid nanogenerator based on zinc ferrite nanorods incorporated poly(vinylidene fluoride-co-hexafluoropropylene) nanocomposite for versatile mechanical energy harvesting. *Mater Res Bull*. 2019;118:110515.

39. Sasmal A, Devi PS, Sen S. Frequency dependent energy storage and dielectric performance of Ba–Zr co-doped $BiFeO_3$ loaded PVDF based mechanical energy harvesters: effect of corona poling. *Soft Matter*. 2020;16:8492-8505.

40. Parangusan H, Ponnamma D, Al-Maadeed MAA. Stretchable electrospun PVDFHFP/co-ZnO Nanofbers as piezoelectric Nanogenerators. *Sci Rep*. 2018;8:754.

41. Barman S, Sikdar S, Biswas A, Mandal BK, Das R. Structural microanalysis of green synthesized $Al_xZn_{(1−x)}O$ nanoparticles. *Nano Express*. 2020;1:020003.

42. Al-Gaashani R et al. XPS and optical studies of different morphologies of ZnO nanostructures prepared by microwave methods. *Ceram Int*. 2013;3:2283-2292.

43. Farsi BA, Souier TM, Marzouqi FA, et al. Rapid microwave-assisted fabrication of Al-doped zinc oxide nanorods on a glass substrate for photocatalytic degradation of phenol under visible light irradiation. *Opt Mater*. 2021;113:110868.

44. Tüzemen ES et al. XRD, XPS, and optical characterizations of Al-doped ZnO film grown on GaAs substrate. *Turk J Phys*. 2014;38:111-117.

45. Sasmal A, Sen S, Devi PS. Role of suppressed oxygen vacancies in the $BiFeO_3$ nanofiller to improve the polar phase and multifunctional performance of poly(vinylidene fluoride). *Phys Chem Chem Phys*. 2019;21:5974-5988.

46. Parangusan H, Ponnamma D, AlMaadeed MAA. Toward high power generating piezoelectric nanofibers: influence of particle size and surface electrostatic interaction of Ce–Fe_2O_3 and Ce–Co_3O_4 on PVDF. *ACS Omega*. 2019;4(4):6312-6323.

47. Kar E, Bose N, Dutta B, Banerjee S, Mukherjee N, Mukherjee S. 2D SnO_2 nanosheet/PVDF composite based flexible, self-cleaning piezoelectric energy harvester. *Energ Conver Manage*. 2019;184:600-608.

48. Zhang C, Fan Y, Li H, et al. Fully Rollable Lead-free poly(vinylidene fluoride)-Niobate-based Nanogenerator with ultra-flexible Nano-network electrodes. *ACS Nano*. 2018;12: 4803-4811.

49. Chen J, Tang Z, Tian R, Bai Y, Zhao S, Zhang H. Domain switching contribution to the ferroelectric, fatigue and piezoelectric properties of lead-free $Bi_{0.5}(Na_{0.85}K_{0.15})_{0.5}TiO_3$ films. *RSC Adv*. 2016;6:33834-33842.

50. Saravanakumar B, Soyoon S, Kim SJ. Self-powered pH sensor based on a flexible organic–inorganic hybrid composite Nanogenerator. *ACS Appl Mater Interfaces*. 2014;6:13716-13723.

51. Park KI, Lee M, Liu Y, et al. Flexible nanocomposite generator made of $BaTiO_3$ nanoparticles and graphitic carbons. *Adv Mater*. 2012;24:2999-3004.

52. Baek C, Yun JH, Wang JE, et al. A flexible energy harvester based on a lead-free and piezoelectric BCTZ nanoparticle–polymer composite. *Nanoscale*. 2016;8:17632-17638.

53. Bagchi B, Hoque NA, Janowicz N, Das S, Tiwari MK. Re-usable self-poled piezoelectric/piezocatalytic films with exceptional energy harvesting and water remediation capability. *Nano Energy*. 2020;78:105339.

54. Bairagi S, Ali SW. A unique piezoelectric nanogenerator composed of melt-spun PVDF/KNN nanorod-based nanocomposite fibre. *Eur Polym J*. 2019;116:554-561.

55. Si SK, Karan SK, Paria S, et al. Khatua BB.A strategy to develop an efficient piezoelectric nanogenerator through ZTO assisted γ-phase nucleation of PVDF in ZTO/PVDF nanocomposite for harvesting bio-mechanical energy and energy storage application. *Mater Chem Phys*. 2018;213:525-537.

56. Joung MR, Xu H, Seo IT, et al. Piezoelectric nanogenerators synthesized using $KNbO_3$ nanowires with various crystal structures. *J Mater Chem A*. 2014;2:18547-18553.

57. Singh HH, Singh S, Khare N. Enhanced β-phase in PVDF polymer nanocomposite and its application for nanogenerator. *PolymAdv Technol*. 2018;29:143-150.

58. Sultana A, Sadhukhan P, Alam M, Das S, Middya R, Mandal D. Organo-lead halide perovskite induced electroactive β-phase in porous PVDF films: an excellent material for photoactive piezoelectric energy harvester and photodetector. *ACS Appl Mater Interfaces*. 2018;10:4121-4130.

59. Qin W, Zhou P, Xu X, et al. High-performance piezoelectric Nanogenerator based on low-entropy structured nanofibers for a multi-mode energy harvesting and self-powered ultraviolet photodetector. *ACS Appl Electron Mater*. 2022;4(6):2970-2978.

60. BairagiS ASW. A hybrid piezoelectric nanogenerator comprising of KNN/ZnO nanorods incorporated PVDF electrospun nanocomposite webs. *Int J Energy Res*. 2020;44:5545-5563.

61. Zhang S, Lin X, Liu H, et al. High-performance flexible piezoelectric nanogenerator based on necklace-like PZT particle chains. *Int J Energy Res*. 2021;45:6213-6226.

62. Cao VA, Kim M, Lee S, et al. Enhanced output performance of a flexible piezoelectric Nanogenerator realized by lithium-doped zinc oxide nanowires decorated on MXene. *ACS Appl Mater Interfaces*. 2022;14:26824-26832.

SUPPORTING INFORMATION

Additional supporting information can be found online in the Supporting Information section at the end of this article.